Systematic and quantitative analysis of residual amplitude modulation in Pound-Drever-Hall frequency stabilization

Article *in* Physical Review A · December 2015

DOI: 10.1103/PhysRevA.92.063809

CITATIONS
27

READS
743

5 authors, including:

Shen Hui
Shanghai Institute of Optics and Fine Mechanics, CAS
21 PUBLICATIONS **67** CITATIONS
SEE PROFILE

Liufeng Li
Wuhan Institute of Physics and Mathematics
16 PUBLICATIONS **134** CITATIONS
SEE PROFILE

Systematic and quantitative analysis of residual amplitude modulation in Pound-Drever-Hall frequency stabilization

Hui Shen,[1,2] Liufeng Li,[1,3,4] Jin Bi,[1,2] Jia Wang,[1,2] and Lisheng Chen[1,2,3,4,*]

[1]*Wuhan Institute of Physics and Mathematics, Chinese Academy of Sciences, Wuhan 430071, China*

[2]*University of Chinese Academy of Sciences, Beijing 100049, China*

[3]*State Key Laboratory of Magnetic Resonance and Atomic and Molecular Physics, Wuhan 430071, China*

[4]*Laboratory of Atomic frequency Standards, Chinese Academy of Sciences, Wuhan 430071, China*

(Received 14 July 2015; published 7 December 2015)

We theoretically analyze the effects of two primary mechanisms of residual amplitude modulation, estimate the resulting frequency instabilities, and discuss relevant experimental countermeasures, providing useful information that are beneficial for the development of ultrastable optical oscillators as well as many precision experiments relying on stable lasers. A Pound-Drever-Hall signal comprising contributions from the birefringence of the electro-optic crystal is derived and used to examine the birefringence-related amplitude modulation and the resultant frequency offset in terms of various experimental parameters. The combined effect of the crystal birefringence and pararsitic étalons is further investigated by dividing the étalons into three representative categories according to their locations in the optical path. The analysis shows that introducing a resonant optical cavity only scales the birefringence-generated amplitude modulation by a constant, thereby lending strong support to the active control scheme using a separate detection path. When a parasitic étalon is added, the active control scheme can still suppress the resultant instability except for the parasitic étalon that is located closely in front of the optical cavity. In this case the étalon produces rather large frequency instability and therefore should be avoided. In addition, numerical calculations are performed to assess the impact of a special situation where the front and end surfaces of an ultrastable optical cavity are potential sources of the parasitic étalon that can strongly couple with the cavity.

DOI: 10.1103/PhysRevA.92.063809 PACS number(s): 42.60.Da, 42.62.Fi, 07.60.Ly, 06.30.Ft

I. INTRODUCTION

Narrow-linewidth lasers obtained with Pound-Drever-Hall (PDH) frequency-locking technique [1] are an essential element for many precision experiments such as laser interferometers [2–5], gravitational wave detectors [6–10], and optical frequency standards [11–17]. In PDH frequency stabilization, an electro-optic modulator (EOM) is usually used to perform the phase modulation in which a residual amplitude modulation (RAM) [18–22] is also generated, resulting in a distorted error signal and systematic frequency shift that will drift under external influences [19,21–24]. As the frequency instability of the ultrastable optical oscillator has been pushed down to the $\leqslant 10^{16}$ range [25,26], it is important to not only comprehensively understand the RAM-inducing mechanisms but also quantitatively evaluate the resulting frequency instabilities.

The major sources of the RAM have been identified as the natural birefringence [18,19,22,27,28] of the electro-optic (EO) crystal and parasitic étalons [23,29–31], along with other contributing mechanisms [24,32,33]. Birefringence-induced RAM was analyzed in detail [22], leading to passive and active RAM-suppression schemes [18–22,28,33–35]. However, the relevant theoretical model concentrated on the RAM presented in the laser beam exiting the birefringent EO crystal [22]. It remains to be seen whether the field leakage from the frequency-locking cavity can dramatically modify the characteristic of RAM, a critical issue that determines the effectiveness of those active control schemes relying on RAM detection in a separate optical path. Being another primary source of RAM, the parasitic étalons [23,29–31] have a wide spread of both their parameters and locations, adding complications to evaluate their impact and take effective countermeasures. Additionally, in most experimental setups the two mechanisms coexist and therefore their combined effect should also be addressed in the theoretical model.

A thorough understanding of RAM and its consequence provides guidance on the analysis of the related systematic effects in ultrastable optical oscillators as well as many precision measurements and systems involving stable lasers. Furthermore, such analysis will be beneficial to the optimization of experimental parameters for a maximum amount of RAM suppression, and aid the development of alternative RAM-reducing approaches not only in the PDH frequency stabilization but also in many other related applications such as frequency modulation spectroscopy (FMS) [21,29,36–39], modulation transfer spectroscopy (MTS) [32,40,41], and noise-immune cavity-enhanced optical heterodyne molecular spectroscopy (NICE-OHMS) [42–44].

We conduct a systematic investigation on the RAM originating from the crystal birefringence and parasitic étalons and quantitatively evaluate the related frequency instabilities in the PDH frequency stabilization. Starting from a generalized signal resulting from an optical component interrogated by a phase-modulated laser beam, the analytical PDH signal is derived with the crystal birefringence taken into consideration, enabling a detailed analysis of the modified PDH error signal and the resultant frequency shift. In addition, the combined effect of the parasitic étalon, the crystal birefringence, and the optical cavity is analyzed by examining three representative locations of a parasitic étalon in the optical path. With further simplification made on the response of the parasitic étalon, the amount of RAM and the resultant frequency instabilities

*Corresponding author: lchen@wipm.ac.cn

for passive and active RAM control schemes are evaluated and compared. For a more complex situation where a parasitic étalon strongly couples with the reference cavity, numerical calculations are performed to evaluate the RAM-induced frequency instabilities caused by the thermal drifts separately experienced by the parasitic étalon and the EO crystal.

Section II prepares for the discussion by introducing a general form of the PDH signal. Section III then derives the analytical form of the PDH error signal in the presence of the crystal birefringence and evaluates the corresponding frequency shift. The parasitic étalon and its interaction with the crystal birefringence are added to the discussion in Sec. IV. In this section we also address a special case where the parasitic étalon strongly couples with the PDH-locking cavity. The major outcomes and important experimental implications are summarized in Sec. V.

II. A GENERALIZED PDH SIGNAL

Let us consider the experimental setup of PDH frequency locking, which is depicted in Fig. 1. When the input and output polarizers P1 and P2 are, respectively, set at angles α and β relative to the crystal z axis, the phase-modulated optical field after polarizer P2 is

$$E_{\mathrm{EOM}} = E_0 e^{i\omega t}[a e^{i(\delta_o \sin \Omega t + \phi_o)} + b e^{i(\delta_e \sin \Omega t + \phi_e)}], \quad (1)$$

where $a = \sin\alpha \sin\beta$ and $b = \cos\alpha \cos\beta$ are alignment factors [19,22]; ω and Ω are the frequencies of optical carrier and phase modulation, respectively; and $\delta_{o,e}$ and $\phi_{o,e}$, respectively, are the modulation index and the phase shift of the lights where the subscripts o and e stand for, respectively, the extraordinary and ordinary lights. Note that the phase shifts ϕ_o and ϕ_e depend sensitively on many external influences such as the beam alignment, ambient temperature, stress-related effects in the EO crystal, and electric field applied to the crystal [18,19,22,28].

The phase-modulated birefringent light described by Eq. (1) impinges upon an optical component such as an optical cavity or an ensemble of atomic or molecular absorbers. The outgoing optical field is photodetected to produce an electrical signal whose detailed derivation is given in Appendix A. This signal is then demodulated with a local signal of $V_{\mathrm{LO}} \cos(\Omega t + \phi_{\mathrm{mod}})$ and low-pass filtered, generating a PDH signal that can be expressed in a generalized form of

$$\begin{aligned} V_{err} =& E_0^2 G_{oe}\{\mathrm{Re}[AF(\omega)F^*(\omega+\Omega) \\ &- A^*F^*(\omega)F(\omega-\Omega)]\cos\phi_{\mathrm{mod}} \\ &- \mathrm{Im}[AF(\omega)F^*(\omega+\Omega) - A^*F^*(\omega)F(\omega-\Omega)] \\ &\times \sin\phi_{\mathrm{mod}} + T_{\mathrm{high}}\}, \end{aligned} \quad (2)$$

where

$$\begin{aligned} A =& a^2 J_0^o J_1^o + b^2 J_0^e J_1^e + ab\left(J_0^o J_1^e + J_0^e J_1^o\right)\cos\Delta\phi \\ &- iab\left(J_0^o J_1^e - J_0^e J_1^o\right)\sin\Delta\phi. \end{aligned} \quad (3)$$

$F(\omega)$ represents the transfer function of the optical component interrogated by the phase-modulated laser, $J_k^{o,e} = J_k(\delta_{o,e})$ ($k = 0, 1$) is the kth-order Bessel function with its parameter being the birefringent modulation indices, $\Delta\phi = \phi_e - \phi_o$ is the phase shift due to the natural birefringence of the crystal, and G_{oe} is the joint gain of the photodetection and demodulation processes. T_{high} in Eq. (2) absorbs all the contributions involving high-order sidebands ($k \geqslant 2$), which contribute through their beats with neighboring harmonics. When the modulation index $\delta_o(\delta_e)$ is on the order of $\sim$1, a typical value often used to optimize the PDH discrimination slope, the dramatically decreasing trend of the high-order Bessel functions indicates that T_{high} is relatively small and can be neglected.

The dispersion ($\sin\phi_{\mathrm{mod}}$) and absorption ($\cos\phi_{\mathrm{mod}}$) terms in Eq. (2) can be selectively detected by adjusting the local phase ϕ_{mod}. With perfect polarization alignment ($\alpha, \beta = 0^\circ$) and a quadrature phase detection ($\phi_{\mathrm{mod}} = 90^\circ$), Eq. (2) is reduced to the standard PDH error signal [45],

$$V_{\mathrm{PDH}} = E_0^2 G_{oe} A \mathrm{Im}[F_r(\omega)F_r{}^*(\omega+\Omega) - F_r{}^*(\omega)F_r(\omega-\Omega)], \quad (4)$$

where $A = J_0{}^e J_1{}^e$. If the photodetection and the subsequent demodulation are performed directly after the EO crystal, then $F_r(\omega) = 1$ and Eq. (2) is greatly simplified to a birefringence-induced RAM of

$$V_{\mathrm{RAM}} = 2E_0^2 G_{oe} ab J_1(M)\sin\Delta\phi, \quad (5)$$

reproducing exactly the result obtained by a previous analysis [22] with $M = \delta_e - \delta_o$ being the difference in the modulation indices of the extraordinary and ordinary lights.

It follows from the current analysis that a diagnostic test can be performed to discriminate between the two primary causes of the RAM. For the test the in-phase detection ($\phi_{\mathrm{mod}} = 0^\circ$) is used to examine the absorption signal. The laser is steered far away from the cavity resonance or, equivalently, a mirror is inserted in front of the cavity, leading to a greatly simplified transfer function of $F(\omega) = 1$ in Eq. (2) and therefore the absence of the birefringence-related absorption signal. Conversely, the parasitic étalon in the optical path produces a nonzero absorption signal that varies with the étalon length, a phenomenon that can be used to locate the étalon by deliberately tilting the suspected component. Once

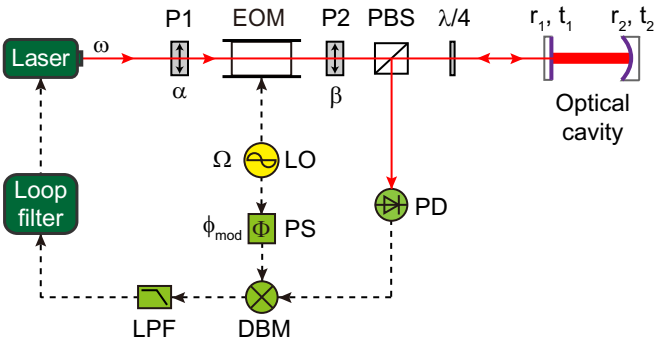

FIG. 1. (Color online) The experimental setup for PDH frequency locking. P1 and P2 are the polarizers aligned, respectively, at angles of α and β to the optical axis of the EO crystal. EOM, electro-optical modulator; PBS, polarization beam splitter; $\lambda/4$, quarter-wave plate; LO, local oscillator; PS, phase shifter; PD, photodetector; DBM, doubly balanced mixer; LPF, low-pass filter. r_i and $t_i (i = 1,2)$ are the reflection and transmission coefficients of the cavity mirrors, respectively.

identified, the parasitic étalon can be eliminated by adjusting the optical alignment with a goal to minimize the absorption signal, which, in the current arrangement, is purely from the étalon effect.

With the birefringence of the EO crystal incorporated, Eq. (2) is rather general in that it describes signals obtained from optical components of different types or from atomic or molecular samples and hence can be employed as an analysis tool in various detection schemes based on the frequency modulation technique. In PDH frequency locking $F(\omega)$ in Eq. (2) is the amplitude reflection coefficient $F_r(\omega)$ of the optical cavity. When there are parasitic étalons in the optical path, $F(\omega)$ is the joint response of the optical cavity and the parasitic étalons.

III. CRYSTAL BIREFRINGENCE

This section analyzes the amount of RAM that arises solely from the birefringence of the EO crystal and the resultant frequency instability. Taking the crystal birefringence into consideration and by working with the transfer function of an optical cavity, we first derive the analytical PDH error signal for a high-finesse optical cavity. Then the birefringence-induced RAM and the corresponding frequency shift are closely examined, followed by discussions on several practical measures for improving the frequency stability. The parasitic étalon and its combined effect with the crystal birefringence will be added to the discussion in Sec. IV.

A. PDH signal with the presence of crystal birefringence

In case of a Fabry-Perot cavity interrogated by a phase-modulated laser beam, the transfer function $F(\omega)$ in Eq. (2) is the amplitude reflection coefficient of the cavity [46–48], which is given by

$$F_r(\omega) = r_1 - \frac{r_2 t_1^2 e^{i\frac{\omega}{\Delta\nu_{\rm FSR}}}}{1 - r_1 r_2 e^{i\frac{\omega}{\Delta\nu_{\rm FSR}}}}, \tag{6}$$

where r_i and t_i are, respectively, the reflection and transmission coefficients of the input ($i = 1$) and end ($i = 2$) mirrors; $\Delta\nu_{\rm FSR}$ is the free spectral range (FSR) of the cavity.

When a high-finesse cavity and fast modulation are used, the reflection coefficient [Eq. (6)] can be approximated to derive explicit expressions for the PDH signal (see Appendix B). The corresponding dispersion and absorption signals in Eq. (2) can be written as

$$V_{\rm dis} \approx -E_0^2 G_{oe} F_{\rm roff}\left(\frac{t_1^2 r_2}{\sqrt{r_1 r_2}(1-r_1 r_2)}{\rm Re}(A)\left[-\frac{2\Delta\omega/(\pi\gamma)}{1+\left(\frac{\Delta\omega}{\pi\gamma}\right)^2}+\frac{(\Delta\omega-\Omega)/(\pi\gamma)}{1+\left(\frac{\Delta\omega-\Omega}{\pi\gamma}\right)^2}+\frac{(\Delta\omega+\Omega)/(\pi\gamma)}{1+\left(\frac{\Delta\omega+\Omega}{\pi\gamma}\right)^2}\right]+{\rm Im}(A)\left\{-\frac{t_1^2(1+r_1r_2)}{2r_1(1-r_1r_2)}\right.$$
$$\left.\times\left[\frac{2}{1+\left(\frac{\Delta\omega}{\pi\gamma}\right)^2}+\frac{1}{1+\left(\frac{\Delta\omega-\Omega}{\pi\gamma}\right)^2}+\frac{1}{1+\left(\frac{\Delta\omega+\Omega}{\pi\gamma}\right)^2}\right]+2F_{\rm roff}\right\}-2F_{\rm roff}[abJ_1(M)\sin\Delta\phi-{\rm Im}(A)]\Bigg)\sin\phi_{\rm mod}, \tag{7}$$

$$V_{abs} \approx E_0^2 G_{oe} F_{\rm roff}\left\{\frac{t_1^2(1+r_1r_2)}{2r_1(1-r_1r_2)}{\rm Re}(A)\left[\frac{1}{1+\left(\frac{\Delta\omega-\Omega}{\pi\gamma}\right)^2}-\frac{1}{1+\left(\frac{\Delta\omega+\Omega}{\pi\gamma}\right)^2}\right]\right.$$
$$\left.+\frac{t_1^2 r_2}{\sqrt{r_1r_2}(1-r_1r_2)}{\rm Im}(A)\left[\frac{(\Delta\omega-\Omega)/(\pi\gamma)}{1+\left(\frac{\Delta\omega-\Omega}{\pi\gamma}\right)^2}-\frac{(\Delta\omega+\Omega)/(\pi\gamma)}{1+\left(\frac{\Delta\omega+\Omega}{\pi\gamma}\right)^2}\right]\right\}\cos\phi_{\rm mod}, \tag{8}$$

where $\gamma = \frac{1-r_1r_2}{\pi\sqrt{r_1r_2}}\Delta\nu_{\rm FSR}$ is the linewidth (full width at half maximum, FWHM) of the cavity, $F_{\rm roff} = r_1(1+\frac{t_1^2}{2r_1^2})$ is the off-resonance reflection coefficient, and $\Delta\omega = 2\pi\Delta\nu$ is the laser detuning with respect to the cavity resonant frequency ω_0. The first term in the dispersion signal is the standard PDH error signal [49,50] and the remaining terms arise out of the birefringence-induced RAM. Being extracted with a demodulation phase of $\phi_{\rm mod} = 90^\circ$ (quadrature detection), the dispersion signal of Eq. (7) is usually used as the error signal to perform the frequency locking.

B. Birefringence-induced frequency shift

Figure 2 shows the central portion of a typical error signal used for frequency locking. Close to the zero crossing the signal can be well approximated by a straight line $V_{err} = D\Delta\nu + V_{\rm RAM} + V_{\rm offset}$, where $\Delta\nu$ is the frequency detuning, D is the discrimination slope, and $V_{\rm RAM}$ denotes the RAM-induced voltage offset. Here a voltage offset $V_{\rm offset}$ introduced by the locking electronics is also taken into consideration. The resultant frequency shift is

$$\Delta\nu_{\rm offset} = -\frac{V_{\rm offset} + V_{\rm RAM}}{D}. \tag{9}$$

According to the explicit form of the PDH error signal [Eq. (7)], the discrimination slope is

$$D = 4E_0^2 G_{oe} F_{\rm roff}\frac{t_1^2 r_2}{\sqrt{r_1r_2}(1-r_1r_2)}\frac{{\rm Re}(A)}{\gamma}\sin\phi_{\rm mod}, \tag{10}$$

and the intercept of the line with the vertical axis is the locking offset, which is evaluated as

$$V_{\rm RAM} = -2E_0^2 G_{oe}{\rm Im}(A)F_{\rm roff}{}^2\left[\frac{F_r(\omega_0)}{F_{\rm roff}}+\frac{J_1^M}{J_0^o J_1^e - J_0^e J_1^o}-1\right]\sin\phi_{\rm mod}$$
$$\approx 2E_0^2 G_{oe} abJ_1(M)F_{\rm roff}F_r(\omega_0)\sin\Delta\phi\sin\phi_{\rm mod}. \tag{11}$$

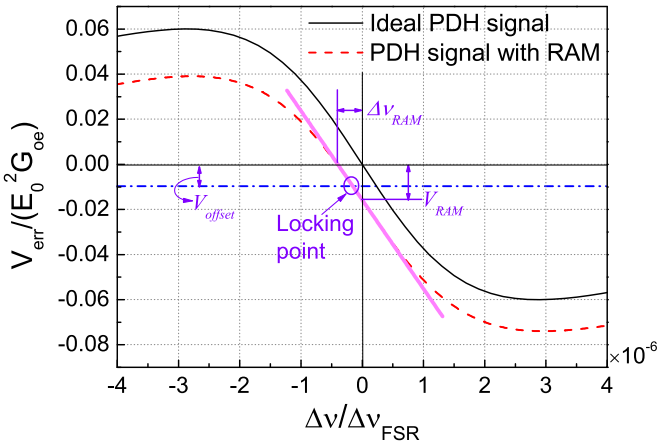

FIG. 2. (Color online) PDH error signal under the influence of the RAM and locking offset. In the vicinity of the zero crossing the signal can be approximated as a straight line with an inclination determined by the PDH discrimination slope. The two intercepts of this line with the vertical and horizontal axes are the dc shift induced by the RAM and the resultant frequency shift, respectively. The frequency-locking system also introduces a voltage offset, which is indicated by the dash-dot line. The actual locking point is the intersection between the error signal and the locking offset.

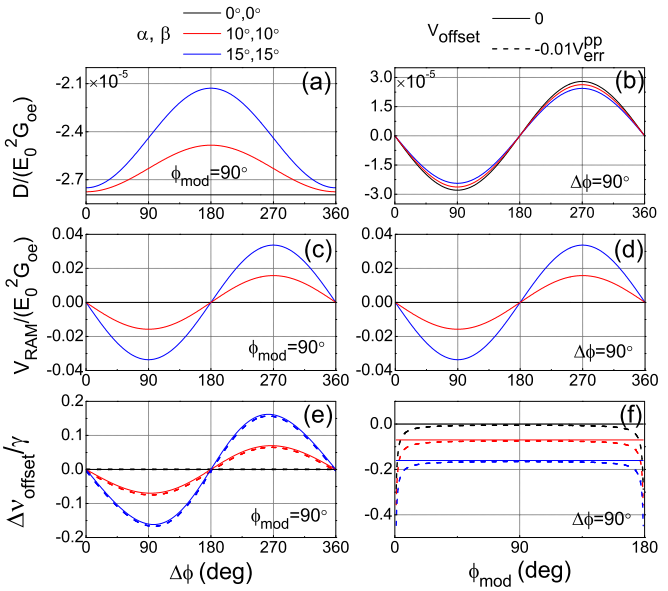

FIG. 3. (Color online) (a,b) The discrimination slope, (c,d) the demodulated RAM signal, and (e,f) the frequency offset as functions of birefringent phase shift $\Delta\phi$ and demodulation phase ϕ_{mod}. A quadrature phase detection ($\phi_{\mathrm{mod}} = 90^\circ$, the dispersion term is detected) is used for birefringent dependences (a,c,e). When the modulation phase (ϕ_{mod}) is adjusted (b,d,f), the birefringence phase shift $\Delta\phi$ is fixed to 90°. In each graph three curves with different polarization angles (α and β, values indicated in the graphs) are plotted. In addition, the effect of adding a locking offset (1% of the peak-to-peak value of the error signal V_{err}^{pp}) is shown in (e,f) with dashed lines.

Equation (11) gives the amount of RAM originating from the crystal birefringence when the interrogated optical cavity is on resonance. $F_r(\omega_0)$ in Eq. (11) is the amplitude reflection coefficient of the resonant cavity and is related to the cavity contrast $C = 1 - F_r{}^2(\omega_0)$. Definitely, using a cavity with high reflection contrast in the PDH frequency locking is an effective way to enhance the immunity to the birefringence-induced RAM.

This derivation [Eq. (11)] also lends strong support to the active control schemes that rely on an independent RAM detection before the light enters the optical cavity [18,19,22,28]. A comparison between Eqs. (5) and (11) shows that introducing a resonant optical cavity only scales the RAM right after the EO crystal by a constant of $F_{\mathrm{roff}}F_r(\omega_0)$, meaning that the detection done prior to the optical cavity accurately maps out the variation of RAM presented in the PDH error signal, thereby ensuring the effectiveness of the active control.

By using Eqs. (9)–(11), the locking frequency offset resulting from the birefringence-induced RAM is evaluated and then closely examined in terms of various experimental parameters, providing valuable observations that are beneficial to the improvement of locking stability. Figure 3 summarizes the results by plotting the variations of the discrimination slope D, the demodulated birefringent RAM, and the frequency offset $\Delta\nu_{\mathrm{offset}}$ in terms of several experimental parameters.

The variation of RAM as a function of birefringent phase shift shown in Fig. 3(c) provides guidance for both passive and active control schemes that operate by stabilizing the birefringent phase shift. When active control is adopted it is advantageous to maintain a phase shift of $\Delta\phi = n\pi$ (n is an integer) because of the readily achievable discrimination signal for RAM control [19]. However, a phase shift of $\Delta f = (2n+1)\pi/2$ can be a better choice for passive stabilization. Despite a maximized dc component, RAM at this phase shift has the smallest rate of change (the variation of RAM per unit change in $\Delta\phi$), facilitating a reduced sensitivity to external perturbations such as temperature and alignment fluctuations.

The potential frequency instability due to an imperfect quadrature detection (ϕ_{mod} departs from a strict 90°) is also investigated. Figures 3(b), 3(d), and 3(f) show the influence of a varying demodulation phase ϕ_{mod} on the discrimination slope D, the RAM, and the locking frequency offset, respectively. Also added in Fig. 3(f) is the effect of a locking-electronics-generated voltage offset (1% of the peak-to-peak value of the error signal V_{err}^{pp}). Under the influence of the electronic offset, a modest departure from the quadrature detection gives rise to a rather small and smoothly varying frequency offset, thereby having negligible influence on the frequency stability. In the calculation the mixture with the absorption signal is considered and will be further explained in the following section (Sec. III C).

C. Mixing with absorption term due to an imperfect quadrature detection

In practical implementation of PDH frequency locking, the demodulation phase is unlikely to be adjusted to and then kept at a strict 90°, resulting in a mixing of the error signal with a small amount of the absorption signal and potentially the same stability-degrading effect as that of a RAM. Here we consider the consequence of an imperfect quadrature detection in the most relevant case of a high-finesse optical cavity interrogated in the fast-modulation regime ($\Omega \gg 2\pi\gamma$).

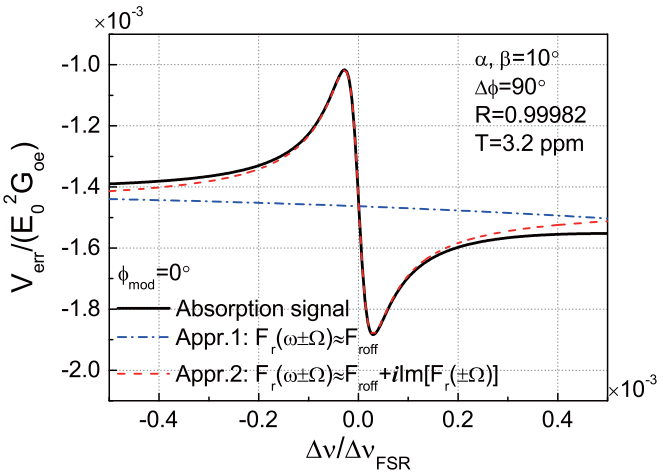

FIG. 4. (Color online) The calculated absorption signal near the resonance of the cavity. In the calculation, the power reflectance and transmittance of the cavity are $R = 0.99982$ and $T = 3.2$ ppm, respectively. Polarization angles are $\alpha, \beta = 10^\circ$ and demodulation phase is $\phi_{\text{mod}} = 0^\circ$. The soild line is the exact solution given by Eq. (2) and the dash-dot and dashed lines are two different approximations using Eqs. (8) and (14), respectively.

Firstly, the approximation adopted in the previous section (Sec. III A) for obtaining the explicit form of the PDH signal is insufficient for a close inspection of the absorption signal in the immediate neighborhood of the cavity resonance. In that derivation the off-resonance reflectance is approximated as a real constant F_{roff}. The corresponding absorption signal is given by Eq. (8) and near the cavity resonance it can be further simplified to

$$V_{abs}(|\Delta\omega| \ll \Omega) = -2E_0^2 G_{oe} F_{\text{roff}} \text{Im}(A) \frac{t_1^2 r_2}{\sqrt{r_1 r_2}(1 - r_1 r_2)} \times \frac{\pi\gamma}{\Omega} \cos\phi_{\text{mod}}, \quad (12)$$

which is on the order of $\text{Im}(A)\frac{\pi\gamma}{\Omega}$ and independent of the laser frequency. Figure 4 shows the behavior of this approximated absorption signal, along with the one numerically calculated by using the exact formula of Eq. (2). Clearly, there is a large difference between the approximated and the exact absorption signals.

For a more precise evaluation of the influence of the absorption signal on the frequency stability, we also retain an imaginary part of the off-resonance reflectance to derive the absorption signal. Here, when $\Delta\omega \to \pm\Omega \gg 2\pi\gamma$, instead of a constant F_{roff}, the reflection coefficient is approximated as $F_r(\omega \pm \Omega) = \text{Re}[F_r(\omega \pm \Omega)] + \text{Im}[F_r(\omega \pm \Omega)]i$ with

$$\text{Re}[F_r(\omega \pm \Omega)] \approx F_{\text{roff}}$$
$$\text{Im}[F_r(\omega \pm \Omega)] \approx \mp \frac{t_1^2 r_2}{\sqrt{r_1 r_2}(1 - r_1 r_2)} \frac{\pi\gamma}{\Omega}. \quad (13)$$

By adding the imaginary part of the off-resonance reflectance, the error signal is derived as

$$V_{err} = E_0^2 G_{oe}\{2\text{Im}[F_r(\Omega)]\text{Im}[AF_r(\omega)]\cos\phi_{\text{mod}} + 2\text{Re}[F_r(\Omega)]\text{Im}[AF_r(\omega)]\sin\phi_{\text{mod}} + T_{\text{high}}\}. \quad (14)$$

The first term in Eq. (14) is the newly derived absorption signal, which is also plotted in Fig. 4. By comparison, near the cavity resonance the new derivation is a good approximation to the exact absorption signal. Now it is sufficient to use Eq. (14) to evaluate the amount of the dispersion component in the error signal due to an imperfect quadrature detection. The result, expressed in terms of the dispersion signal, can be written as

$$V_{abs} = V_{\text{dis}} \frac{-t_1^2 r_2}{F_{\text{roff}}\sqrt{r_1 r_2}(1 - r_1 r_2)} \frac{\pi\gamma}{\Omega} \cot\phi_{\text{mod}}. \quad (15)$$

By only slightly modifying the discrimination slope in the PDH error signal, the mixture does not change the location of the zero crossing of the error signal. As a result, the contamination from the absorption signal has a negligible influence on the frequency stability, as long as the cavity linewidth γ is kept orders of magnitude below the modulation frequency Ω and a fairly good quadrature detection is maintained.

IV. PARASITIC ÉTALON AND ITS INTERPLAY WITH THE BIREFRINGENCE OF THE EO CRYSTAL

This section discusses the combined effect of the parasitic étalon and the birefringence of the EO crystal. The quantitative analysis is made possible by dividing parasitic étalons into three representative categories, aiming at identifying the most significant contribution and providing useful guidance for various RAM-control schemes. We also numerically analyze a special case where the parasitic étalon is embedded in the optical cavity and the two can strongly interact.

A. Three categories of a parasitic étalon

In practice, the parasitic étalons distribute across the entire optical setup and their parameters such as reflectivity and FSR cover a relatively large range that is usually not well determined. To simplify the analysis and still retain generality, we divide the étalons into three representative categories. Figure 5 shows three typical locations of a parasitic étalon in the optical path. The possible locations at which the active RAM control can be implemented are also illustrated in Figs. 5(a) and 5(b). In case (a) the étalon is outside the path where the incoming and reflected laser beams coexist. When the parasitic étalon is located between the PBS and the quarter-wave plate [case (b)], the light directly reflected by the étalon (including its front and rear surfaces) does not enter the photodetector (PD). In case (c) the étalon lies between the quarter-wave plate and the optical cavity. Now the reflections from both the parasitic étalon and the optical cavity are detected, resulting in a mixture of the PDH error signal and the étalon-generated RAM.

The combined effect of the crystal birefringence and a parasitic étalon belonging to each of the three cases can be investigated with the help of Eq. (2) in which $F(\omega)$ is the joint response of the étalon and the optical cavity. Here and in the next section (Sec. IV B) we assume that the parasitic étalon does not couple with the frequency-locking cavity (for the coupled case, see Sec. IV C). Without coupling, the joint responses for three cases take relatively simple forms, which are listed in Table I. Appendix C gives the expressions of RAM for three cases, obtained by substituting $F(\omega)$ in Eq. (2)

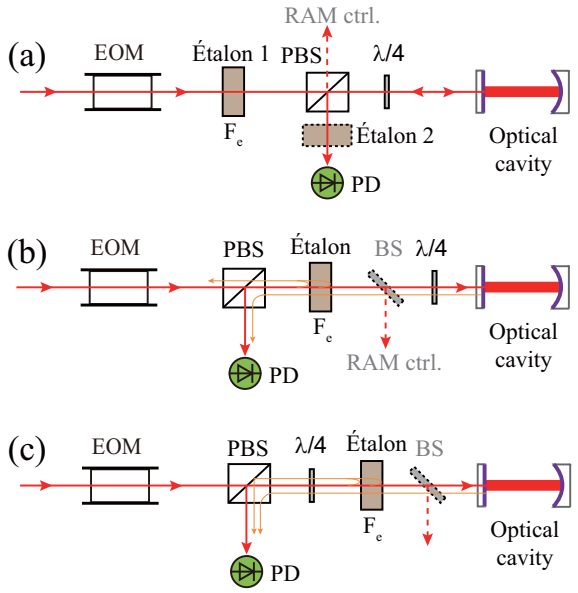

FIG. 5. (Color online) Three representative cases of a parasitic étalon in the PDH optical path. (a) The parasitic étalon is placed between the EOM and PBS or PBS and PD where the light passes the étalon only once. (b) The reflection from the parasitic étalon is not detected due to the polarization mismatch. (c) Reflections from both the parasitic étalon and the optical cavity are detected. Locations for implementing active RAM suppression are illustrated in (a,b).

with the corresponding transfer function listed in Table I. The expressions of RAM obtained up to now are rather general in that they do not involve the explicit form of the étalon transfer function, which will be introduced in the next section (Sec. IV B) to evaluate the resultant frequency instability.

It is worth noting that, by inspecting the general expressions [Eqs. (C1)–(C5)] of RAM, using an optical cavity with high reflection contrast boosts the immunity to RAM in cases (a) and (b), a feature that has already been shown when there is only birefringence-induced RAM (Sec. III B). However, this immunity is not available for case (c) because the corresponding RAM has two additional contributions [Eqs. (C4) and (C5)] that cannot be scaled down by decreasing $F_r(\omega_0)$.

B. RAM-induced frequency instabilities

Here we make a further approximation on the transfer function of the parasitic étalon to give an order-of-magnitude estimation of the frequency instabilities in three cases

TABLE I. The joint transfer function of a parasitic étalon and the optical cavity.

	$F(\omega)$[a]
Case (a)	$F_{et}(\omega)F_r(\omega)$
Case (b)	$F_{et}(\omega)^2F_r(\omega)$
Case (c)	$F_{er}(\omega)+F_{et}(\omega)^2F_r(\omega)$

[a] $F_{er}(\omega)$ and $F_{et}(\omega)$ are, respectively, the reflective and transmissive responses of the parasitic étalon and $F_r(\omega)$ is the response of the cavity for PDH frequency locking. Figure 5 illustrates the locations of the parasitic étalon in cases (a–c).

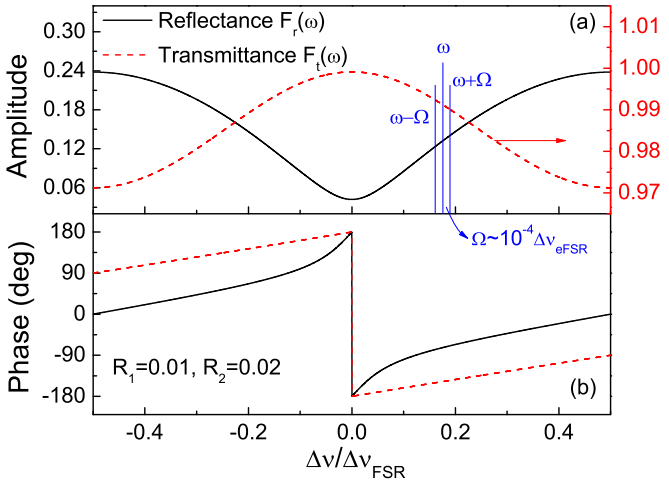

FIG. 6. (Color online) (a) Amplitude and (b) phase responses of a parasitic étalon (a low-finesse optical cavity). When the modulation frequency Ω is much smaller than the FSR of the étalon, the frequency dependence of the responses is approximately linear in the frequency range spanned by the two sidebands ($\omega \pm \Omega$).

discussed in the previous section (Sec. IV A) and make quantitative comparisons between passive and active RAM-control schemes.

1. Frequency response of a parasitic étalon

In contrast to a high-finesse cavity used for frequency locking, a typical parasitic étalon has a low reflectance of below 1%, resulting in slowly varying transmission and reflection versus optical frequency. In particular, those étalons with thickness less than ∼10 mm are of more significance in our analysis because longer ones can be effectively removed by tilting the associated optical components. Accordingly, we assume in the following analysis that the modulation frequency Ω is much less than the FSR of the parasitic étalon. Figure 6 gives such an example by plotting the response of a low-finesse cavity, together with the interrogating optical carrier and its sidebands. As the effective length of the étalon drifts under the environmental influence, the carrier and its two sidebands spend most of their time on the same side of a transmission or reflection crest. It then follows that in the frequency range defined by the two sidebands the transfer functions $F_{et}(\omega)$ (transmission) and $F_{er}(\omega)$ (reflection) are approximately linear and can be written as

$$\begin{aligned} F_{et}(\omega_0 \pm \Omega) &\approx (F_{et0} \pm \varepsilon_t)e^{i(\Phi_{et0}\pm\xi_t)}, \\ F_{er}(\omega_0 \pm \Omega) &\approx (F_{er0} \pm \varepsilon_r)e^{i(\Phi_{er0}\pm\xi_r)}, \end{aligned} \tag{16}$$

where F_{et0} (Φ_{et0}) and F_{er0} (Φ_{er0}) are the amplitudes (phases) at the carrier frequency and $\varepsilon_{t,r}$ ($\xi_{t,r}$) account for the small amplitude (phase) differences between the sidebands and the carrier. In the following discussion these approximated transfer functions are used to evaluate the amount of RAM produced by the crystal birefringence and a parasitic étalon in one of the three cases.

2. Free-running RAM

The RAM-generated voltage offsets in three cases introduced in Sec. IV A are evaluated by using the approxi-

mated transfer functions [Eq. (16)] and Eqs. (C1)–(C5) in Appendix C. Note that for the current evaluation the parameter A defined in Eq. (3) is reduced to $A \approx A_0 + iA_2 \sin\Delta\phi$ with $A_0 = a^2 {J_0}^o {J_1}^o + b^2 {J_0}^e {J_1}^e$ and $A_2 = ab({J_0}^o {J_1}^e - {J_0}^e {J_1}^o)$. The evaluated voltage offsets in cases (a) and (b) are given by

$$V_{\mathrm{RAM}a} \approx -E_0^2 G_{oe} \sin\phi_{\mathrm{mod}} F_{\mathrm{roff}} F_r(\omega_0) \times 2{F_{et0}}^2 \left(A_2 \cos\xi_t \sin\Delta\phi - \frac{\varepsilon_t}{F_{et0}} A_0 \sin\xi_t \right) \quad (17)$$

and

$$V_{\mathrm{RAM}b} \approx -E_0^2 G_{oe} \sin\phi_{\mathrm{mod}} F_{\mathrm{roff}} F_r(\omega_0) \times 2{F_{et0}}^4 \left(A_2 \cos 2\xi_t \sin\Delta\phi - \frac{2\varepsilon_t}{F_{et0}} A_0 \sin 2\xi_t \right), \quad (18)$$

respectively. The signal in case (c) can be written as

$$V_{\mathrm{RAM}c} \approx V_{\mathrm{RAM}b} + V_{\mathrm{RAM}r} + V_{\mathrm{RAM}rt}, \quad (19)$$

where the first term on the right-hand side is the same as the signal in case (b) and the last two terms are given by

$$V_{\mathrm{RAM}r} \approx -2E_0^2 G_{oe} \sin\phi_{\mathrm{mod}} {F_{er0}}^2 \times \left(A_2 \cos\xi_r \sin\Delta\phi - \frac{\varepsilon_r}{F_{er0}} A_0 \sin\xi_r \right), \quad (20)$$

$$V_{\mathrm{RAM}rt} \approx -2E_0^2 G_{oe} \sin\phi_{\mathrm{mod}} F_{er0} {F_{et0}}^2 \times \{ [F_{\mathrm{roff}} \cos 2\xi_t - F_r(\omega_0)\cos\xi_r] \sin\Delta\Phi_{rt} A_0 + [F_{\mathrm{roff}} \cos 2\xi_t + F_r(\omega_0)\cos\xi_r] \times \cos\Delta\Phi_{rt} A_2 \sin\Delta\phi \}, \quad (21)$$

where $\Delta\Phi_{rt} = \Phi_{er0} - 2\Phi_{et0}$.

3. RAM with active control

An active control scheme can be implemented by detecting RAM in a separate path before light enters the cavity [18,19,22,28], as illustrated in Fig. 5. The demodulated signal used for the feedback control is given by

$$V_{\mathrm{RAM}sep} \approx -2E_0^2 G_{oe} \sin\phi_{\mathrm{mod}} F_{\mathrm{roff}} {F_{et0}}^2 \times \left(A_2 \cos\xi_t \sin\Delta\phi - \frac{\varepsilon_t}{F_{et0}} A_0 \sin\xi_t \right). \quad (22)$$

The feedback mechanism forces $V_{\mathrm{RAM}sep}$ to zero by adjusting the birefringence phase shift $\Delta\phi$ to satisfy the condition

$$\sin\Delta\phi = \tan\xi_t \frac{A_0\varepsilon_t}{A_2 F_{et0}}. \quad (23)$$

The RAM in the PDH-locking path, which originates from both crystal birefringence and parasitic étalons, is completely suppressed when the parasitic étalon is located between the EOM and PBS [étalon 1, Fig. 5(a)] because $V_{\mathrm{RAM}a}$ [Eq. (17)] is the same as $V_{\mathrm{RAM}sep}$ except for a constant $F_r(\omega_0)$. For the étalon outside the path shared by the RAM detection and frequency locking [étalon 2, Fig. 5(a)], the birefringence phase shift $\Delta\phi$ is still nulled by the active control. Therefore the contribution from the crystal birefringence is removed and the RAM is solely from the étalon effect, which leads to a residual frequency instability of

$$\Delta\nu^{act}_{\mathrm{RAM}a2} \approx \frac{1}{2} \frac{\sqrt{r_1 r_2}(1 - r_1 r_2)}{t_1^2 r_2} \frac{1}{{J_0}^e {J_1}^e} A_0 F_r(\omega_0) F_{et0} \varepsilon_t \xi_t \gamma. \quad (24)$$

To examine the behavior of the active control in cases (b) and (c), the corresponding frequency instabilities are evaluated by applying the condition of Eq. (23) to Eqs. (18)–(21), yielding

$$\Delta\nu^{act}_{\mathrm{RAM}b} \approx \frac{3}{2} \frac{\sqrt{r_1 r_2}(1 - r_1 r_2)}{t_1^2 r_2} \frac{1}{{J_0}^e {J_1}^e} A_0 F_r(\omega_0) {F_{et0}}^3 \varepsilon_t \xi_t \gamma, \quad (25)$$

and

$$\Delta\nu^{act}_{\mathrm{RAM}c} = \Delta\nu^{act}_{\mathrm{RAM}b} + \Delta\nu^{act}_{\mathrm{RAM}r} + \Delta\nu^{act}_{\mathrm{RAM}rt}, \quad (26)$$

$$\Delta\nu^{act}_{\mathrm{RAM}r} \approx -\frac{1}{2} \frac{\sqrt{r_1 r_2}(1 - r_1 r_2)}{t_1^2 r_2} \frac{1}{F_{\mathrm{roff}}} \frac{1}{{J_0}^e {J_1}^e} A_0 \times {F_{er0}}^2 \left(\frac{\varepsilon_t}{F_{et0}} \cos\xi_r \tan\xi_t - \frac{\varepsilon_r}{F_{er0}} \sin\xi_r \right) \gamma, \quad (27)$$

$$\Delta\nu^{act}_{\mathrm{RAM}rt} \approx -\frac{1}{2} \frac{\sqrt{r_1 r_2}(1 - r_1 r_2)}{t_1^2 r_2} \frac{1}{{J_0}^e {J_1}^e} A_0 F_{er0} {F_{et0}}^2 \times \left\{ \left[\cos 2\xi_t - \frac{F_r(\omega_0)}{F_{\mathrm{roff}}} \cos\xi_r \right] \sin\Delta\Phi_{rt} + \left[\cos 2\xi_t + \frac{F_r(\omega_0)}{F_{\mathrm{roff}}} \cos\xi_r \right] \frac{\varepsilon_t}{F_{et0}} \tan\xi_t \cos\Delta\Phi_{rt} \right\} \gamma. \quad (28)$$

In cases (b) and (c), $V_{\mathrm{RAM}sep}$, the signal detected before light enters the cavity, no longer fully represents the RAM in the frequency-locking path, resulting in additional contributions when the active control is implemented. Next, we use typical parameters of a parasitic étalon and their variations to estimate the resultant frequency instabilities and examine the effectiveness of various RAM-control schemes.

4. Comparison among different stabilization approaches

Table II summarizes our order-of-magnitude estimation of the frequency instabilities originating from the birefringence of the EO crystal and a parasitic étalon in one of the three cases discussed in Sec. IV A. In each case we evaluate the instabilities for three stabilization approaches. Firstly, the EO crystal is temperature controlled to stabilize the birefringent phase shift. Then the active control using a separate detection path is implemented. Last, without using active control, the influence of the crystal birefringence is eliminated by using only one of the two polarization components. Parasitic étalons with length L_e ranging from 1 to 100 mm are considered in the calculation and for all étalons the coefficients of the reflectance are fixed to $R_1 = 0.01$ and $R_2 = 0.02$ for the front and rear surfaces, respectively. We use the maximum possible variations of the étalon parameters, which are explained below

TABLE II. RAM-induced frequency instabilities in three cases with the length of the parasitic étalon in the range of 1–100 mm.[a]

		Without active control[b]	Active control	No crystal birefringence
Case (a)	Étalon 1	$10^{-4}\gamma$	0	$(10^{-9}-10^{-5})\gamma$
	Étalon 2	$10^{-4}\gamma$	$(10^{-9}-10^{-5})\gamma$	$(10^{-9}-10^{-5})\gamma$
Case (b)		$10^{-4}\gamma$	$(10^{-8}-10^{-4})\gamma$	$(10^{-8}-10^{-4})\gamma$
Case (c)		$10^{-1}\gamma$	$10^{-1}\gamma$	$10^{-1}\gamma$

[a]Reflectance of all étalon surfaces is fixed to $R_1 = 0.01$ and $R_2 = 0.02$. The maximum allowable variations of the étalon parameter ε_t are $\Delta\varepsilon_t = 8 \times 10^{-6}$ and 8×10^{-4} for $L_e = 1$mm and 100 mm, respectively, and $\Delta\Phi_{rt}$ takes all possible values from $-\pi$ to π. ξ_t is fixed to 2×10^{-4} rad and 2×10^{-2} rad for $L_e = 1$ mm and 100 mm, respectively. Contributions related to ε_r and ξ_r are orders of magnitude smaller and hence neglected. Other parameters include the modulation frequency $f_m = 10$ MHz, polarization angles $\alpha, \beta = 3^\circ$, and birefringent modulation indices $\delta_o = -0.4$ and $\delta_e = -1.1$. γ denotes the linewidth of the high-finesse cavity whose reflection contrast is 33%[$F_r(\omega_0) = 0.8$].

[b]The MgO:$LiNbO_3$ (MgLN) crystal is assumed in the calculation. The temperature dependence of $\Delta\phi$ is 8 rad/K [19], resulting in a birefringence phase fluctuation of 0.008 rad when the thermal stability of the EO crystal is 1 mK.

Eqs. (16) and (21) and in Table II, to calculate the frequency instabilities by using Eqs. (17)–(21) and Eqs. (24)–(28).

In case (a) the active control completely suppresses the frequency instability when the parasitic étalon is inside the path shared by the RAM detection and frequency locking [étalon 1, Fig. 5(a)]. Although limited to only a subset of parasitic étalons that belong to case (a), in practice this effectiveness holds great significance. Parasitic étalons in this subset are usually distributed in a relatively long optical path in which an increased number and a large variety of the optical components can be found, restricting the effectiveness of passive stabilization.

If a parasitic étalon either locates outside the common path in case (a) or belongs to case (b), then the RAM-induced frequency instability is also greatly reduced by implementing active control, provided that only thin étalons with centimeter to millimeter thickness or thinner are involved. Given the same reflectance of their surfaces, a thin étalon creates a smaller amount of RAM compared with a thick one. As a result, the RAM is primarily caused by the birefringence of the EO crystal and hence suppressed by the active control, resulting in only small residual instability introduced by the thin étalon. As the length of the parasitic étalon is progressively increased to 100 mm and beyond, the active control becomes less effective and then ceases to function. In practice this limitation poses no difficulty either because the strength of the interference in a thicker étalon can be more effectively suppressed by tilting the étalon, or because a long parasitic étalon is usually formed by reflecting surfaces in different components and thus can be removed by making the related components out of alignment.

The étalon effect dominates in case (c) and creates a large frequency instability. In this case the light registered by the PD has its origins of two fields that are either directly reflected by the étalon or from the optical cavity [cf. Fig. 5(c)], the latter consisting of both the reflection at the front surface of the cavity and a leakage field. The interference between these two fields results in the largest contribution [Eq. (28)] that is not present in the RAM sensing path and therefore cannot be removed by active control. Consequently, the parasitic étalon located between the quarter-wave plate and the cavity should be avoided in the first place. One of the potential parasitic étalons of this category is the optical window on the vacuum chamber housing the cavity. In addition to antireflection (AR) coatings and wedged or tilted components, one can also rearrange the optical layout to bring the offensive optical components out of the path between the quarter-wave plate and the cavity [26], converting the unwanted étalons to manageable ones that belong to case (b).

TABLE III. RAM-induced frequency instabilities for three types of EO crystal with only temperature stabilization.[a]

	$LiTaO_3$ (LT)	$NH_4H_2PO_4$ (ADP)	KH_2PO_4 (KDP)
Case (a)	$10^{-3}\gamma$	$10^{-4}\gamma$	$10^{-5}\gamma$
Case (b)	$10^{-3}\gamma$	$10^{-4}\gamma$	$10^{-5}\gamma$
Case (c)	$10^{-1}\gamma$	$10^{-1}\gamma$	$10^{-1}\gamma$

[a]The frequency instabilities are evaluated using the same set of parameters given in Table II, except for the thermal sensitivities of the birefringence phase shift $\Delta\phi$, which are 83 rad/K, 16 rad/K, and 3.5 rad/K for LT, ADP, and KDP crystals, respectively [51,52]. The residual thermal fluctuation of the EO crystals is assumed to be 1 mK.

To examine the contributions solely from the étalon effect, we set the polarization angles α, β to zero and calculate the corresponding frequency instabilities, which are given in the last column of Table II. In cases (b) and (c) the achievable frequency stabilities are on the same level with those obtained by implementing the active control scheme, indicating that the active control has removed the contribution from the crystal birefringence, leaving only the étalon effect untouched.

Without active control, the RAM-induced frequency instability depends on the type of the EO crystal. The relevant result for MgLN crystal can be found in Table II, and Table III adds corresponding frequency instabilities for $LiTaO_3$ (LT), $NH_4H_2PO_4$ (ADP), and KH_2PO_4 (KDP) crystals, all of which are assumed to experience a 1-mK thermal fluctuation in the calculation. Among the four crystals, the frequency instability with LT is relatively large, whereas KDP contributes the smallest instability in cases (a) and (b). When the active control is adopted, the residual RAM is dominated by the étalon effect and therefore the corresponding frequency instability (cf. Table II) is the same for different EO crystals.

However, it should be noted that the theoretically predicted performance may not be fully realized in practice because the fidelity of the detected RAM can be degraded by several factors such as the uncorrelated front-end electronic noises in different feedback control loops, the hidden parasitic étalons outside the optical path shared by the RAM detection and frequency locking, and the inhomogeneous spatial RAM distribution [19,28]. Nevertheless, the effectiveness of the active control can be improved by optimizing the optical alignment, reinforcing the mechanical structure, and avoiding aperture stops in the optical path.

The above analysis concentrates on three representative cases of a single étalon. Although not covered in the present discussion, multiple and distributed parasitic étalons can be quantitatively analyzed in a similar manner to expedite the identification and elimination of the most significant contributions.

C. Parasitic étalons strongly coupling with the frequency-locking cavity

In the above analysis the parasitic étalons do not couple with the optical cavity, an assumption that is valid in most situations where optical components can be deliberately tilted to misalign the parasitic étalons. However, some special optical configurations are more prone to a strong coupling. Figure 7 illustrates such an example in which the input and output surfaces of a high-finesse optical cavity are possible sources of parasitic étalons that are coaxial with the optical cavity. In practice, strict parallelism is avoided for the two end surfaces of the mirror substrate and AR coatings with residual reflectance below 0.001 are used. Nevertheless, a quantitative analysis for the strong-coupling case is still desirable in order to not only evaluate the frequency instability for existing systems but also assist in designing the ultrastable optical cavities.

To proceed we consider two possible configurations in which either the input or output surface couples with the two high-reflecting surfaces in a high-finesse optical cavity (cf. Fig. 7), forming a three-mirror cavity. Equation (2) can still be used to calculate the PDH error signal by noting that the $F(\omega)$ is the three-mirror-cavity transfer function, which is derived by using the method detailed in Ref. [48]. Due to the increased complexity of the transfer function, numerical calculations are performed to obtain the worst-case estimation

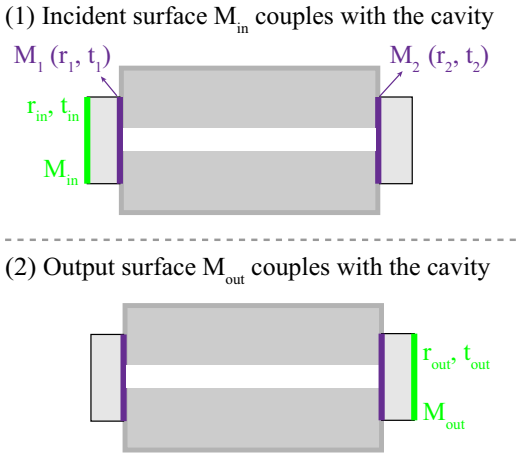

FIG. 7. (Color online) Parasitic étalons in a high-finesse optical cavity. Two possibilities are considered in the main text; i.e., either (a) the input surface (M_{in}) or (b) the output surface (M_{out}) couples with the two high-reflecting surfaces (M_1 and M_2) to form a three-mirror cavity. The transfer functions of the resulting three-mirror cavities are obtained in a recursive manner [47]. First, two neighboring mirrors are selected to form a cavity, which is then treated as an effective mirror, using the reflection and transmission of the newly formed cavity. Then this process is repeated for the effective mirror and the third mirror to obtain the transfer function of the three-mirror cavity.

TABLE IV. The parameters used in the numerical calculation for a reflecting surface coupling with the high-finesse cavity.[a]

Reflectance and transmittance	$R = 0.999982$, $T = 3.2$ ppm
FSR	FSR = 1.5 GHz
Contrast	C = 33%
Normalized discrimination slope $[D/4E_0^2G_{oe}$; see Fig. 4(a)]	$D_1 = 2.79 \times 10^{-5}$
Thickness of the mirror substrates	$L_e = 5$ mm
Reflectance of the input surface	$R_{\text{in}} = 0.001$

[a]Other parameters are the laser wavelength of 1064 nm, the modulation frequency of $f_m = 10$ MHz, the demodulation phase of $\phi_{\text{mod}} = 90^\circ$, and the polarization angles of $\alpha, \beta = 3^\circ$.

of the resultant frequency instability based on a set of typical experimental parameters, which are listed in Table IV. Moreover, we separately evaluate the contributions from the étalon effect and the crystal birefringence by introducing a 1-mK thermal fluctuation on the mirror substrate while keeping the temperature of the EO crystal constant and vice versa. The result of the second configuration (the output surface couples with the cavity) is similar to that of the first one and is omitted in the following discussion.

Table V gives the frequency instability caused by the thermal fluctuation of the mirror substrate. In the calculation the reflectance of the input surface is $R_{in} = 0.001$ and the birefringence phase shift is fixed to $\Delta\phi = 2^\circ$. When the laser is locked to the optical cavity, the RAM-induced frequency shift exhibits approximately sinusoidal dependence on the FSR of the parasitic étalon with a maximum slope of 6.86×10^{-5} Hz/Hz, leading to a worst-case frequency instability on the order of $\sim 10^{-17}$ mK^{-1} for both ultra-low expansion glass (ULE) and fused silica substrates. This frequency instability is due primarily to the thermal dependence of the refractive index of the mirror substrate.

The calculation shows that in this coupled case the frequency shift also has an approximately sinusoidal dependence on the birefringence phase shift $\Delta\phi$. Table VI gives the frequency instabilities induced by the change in the phase shift $\Delta\phi$ when the EO crystal (MgLN) experiences a 1-mK thermal fluctuation. In the calculation the maximum susceptibility (Table V) to the phase shift $\Delta\phi$ is chosen to obtain the worst-case estimation, which shows a relatively large frequency instability of $\sim 10^{-16}$ mK^{-1} compared with the contribution from the étalon effect.

The above calculations indicate that in the worst case the parasitic étalons within a high-finesse optical cavity pose a potential barrier for obtaining ultrastable lasers with 10^{-16}-level frequency stability. As a countermeasure and in addition to high-performance AR coatings, a wedge angle for both the input and output mirrors may be necessary to further suppress the interference inside each mirror substrate.

V. CONCLUSION

The RAM originating from the birefringence of the EO crystal and the parasitic étalon is systematically investigated to evaluate their impact on ultrastable lasers referenced to high-finesse optical cavities. By deriving the PDH signal under

TABLE V. Frequency instability (fractional) caused by the thermal fluctuation of the mirror substrate when a parasitic étalon strongly couples with the cavity.[a]

	ULE substrate	Fused silica substrate
Coefficient of thermal expansion	$1 \times 10^{-8}\,\mathrm{K}^{-1}$	$5 \times 10^{-7}\,\mathrm{K}^{-1}$
Refractive index	1.48	1.45
Thermal coefficient of the reflective index	$1.1 \times 10^{-5}\,\mathrm{K}^{-1}$	$9.6 \times 10^{-6}\,\mathrm{K}^{-1}$
RAM-induced frequency instability	$3.6 \times 10^{-17}\,\mathrm{mK}^{-1}$	$3.4 \times 10^{-17}\,\mathrm{mK}^{-1}$

[a]The AR-coated surface (residual reflection $R_{in} = 0.001$) of the input mirror couples with the two high-reflecting surfaces of the cavity. The thickness of the mirror substrate is $L_e = 5$ mm (FSR = 20 GHz). The birefringence phase shift is fixed to $\Delta\phi = 2^\circ$.

the influence of the birefringence of the EO crystal, it is verified that birefringence-induced RAM in the PDH error signal is the same as what is detected before light enters the cavity except for a constant scaling factor related to the reflection contrast of the cavity. The overall effect caused by the birefringence of the EO crystal and a parasitic étalon is analyzed by considering three representative locations of the parasitic étalon in the frequency-locking system. The corresponding RAMs and resultant frequency instabilities are evaluated, allowing comparisons among three approaches of (1) passive stabilization, (2) active RAM control, and (3) eliminating one of the two birefringent beams. We also discussed a special case that an étalon strongly couples with the frequency-locking cavity. When a parasitic étalon with reflecting surface of $R = 0.001$ couples with the optical cavity, the fractional frequency instabilities due to the thermal fluctuations of the EO crystal and the substrate are evaluated to be on the orders of 10^{-16} and $10^{-17}\,\mathrm{mK}^{-1}$, respectively.

Based on the previous and current analyses, a series of measures can be adopted for coping with the RAM-related instability. Firstly, improving the contrast of the cavity reflection will definitely lead to a reduced susceptibility to RAM [28] and other measurement noises [49]. Furthermore, in most situations, RAM can be monitored separately before the light enters the cavity and feedback control can be adopted to suppress RAM. However, if a parasitic étalon is located in places between the quarter-wave plate and the cavity, it induces a relatively large frequency instability that cannot be suppressed by the active control and therefore the étalon has to be avoided. In summary, the active control of RAM using a separate detection path is an effective approach to suppress RAM with minor modifications to the existing optical layout. To reach its full potential, the differential effects in the RAM sensing and frequency-locking paths should be kept as low as possible. It should be also noted that an alternative method has already been adopted to spatially separate the two polarization components in the EO crystal and subsequently use only one component to perform the frequency locking [34,35]. Nevertheless, in this approach the effect of the parasitic étalons and the possibility of additional RAM-inducing process remain to be further analyzed.

The theoretical models developed thus far allow systematic investigations on RAM-related effects in the development of ultrastable optical oscillators with 10^{-17}-level stability for the next-generation optical clocks. Moreover, similar analyses are beneficial to the performance evaluation and optimization in many other research areas such as high-precision laser spectroscopy and laser interferometry in which the frequency modulation technique is widely adopted.

TABLE VI. Frequency instability (fractional) caused by the birefringence phase fluctuation of the EO crystal (MgLN) when a parasitic étalon strongly couples with the cavity.[a]

Polarization angles	$\alpha,\beta = 3^\circ$	$\alpha,\beta = 1^\circ$
Temperature dependence of $\Delta\phi$ [19]	8 rad/K	8 rad/K
Maximum susceptibility to $\Delta\phi$	33.4 Hz/rad	3.8 Hz/rad
RAM-induced frequency instability	$9.5 \times 10^{-16}\,\mathrm{mK}^{-1}$	$1.1 \times 10^{-16}\,\mathrm{mK}^{-1}$

[a]The AR-coated surface (residual reflection $R_{\mathrm{in}} = 0.001$) of the input mirror couples with the two high-reflecting surfaces of the cavity. The length of the EO crystal is 35 mm.

ACKNOWLEDGMENTS

This work is supported by the National Basic Research Program of China (Grant No. 2012CB821303) and the National Science Foundation of China (Grants No. 11235004 and No. 11327407).

APPENDIX A: OUTPUT OF AN OPTICAL COMPONENT INTERROGATED BY A PHASE-MODULATED LIGHT WITH IMPRINTS OF THE BIREFRINGENCE OF THE EO CRYSTAL

When a phase-modulated light described by Eq. (1) is used to interrogate an optical component, in the time domain the output field is a convolution of the input field and the response of the optical component, i.e.,

$$E_{\mathrm{out}} = E_{\mathrm{EOM}} \otimes f(t). \tag{A1}$$

The convolution gives, on substituting from Eq. (1),

$$\begin{aligned} E_{\mathrm{out}} &= E_{\mathrm{EOM}} \otimes f(t) = E_o + E_e \\ &= E_0 \sum_{n=-\infty}^{+\infty} F(\omega + n\Omega)\left(a e^{i\phi_o} J_n^o + b e^{i\phi_e} J_n^e\right) e^{i(\omega+n\Omega)t}, \end{aligned} \tag{A2}$$

where

$$\begin{pmatrix} E_o \\ E_e \end{pmatrix} = E_0 \begin{pmatrix} a e^{i\phi_o} \\ b e^{i\phi_e} \end{pmatrix} \sum_{n=-\infty}^{+\infty} F(\omega + n\Omega) \begin{pmatrix} J_n^o \\ J_n^e \end{pmatrix} e^{i(\omega+n\Omega)t}, \tag{A3}$$

and $F(\omega)$ is the Fourier transform of $f(t)$.

A subsequent photodetection generates a current that is proportional to the power of the output light, which can be decomposed to

$$E_{\text{out}}E_{\text{out}}^{*} = E_o E_o^{*} + E_e E_e^{*} + E_o E_e^{*} + E_o^{*} E_e, \tag{A4}$$

where the first two terms on the right-hand side produce the standard PDH error signal and the remaining cross terms give rise to the amount of RAM originating from the birefringence of the EO crystal. Here, we consider the case that the signal is demodulated at the fundamental frequency. By using Eq. (A3), the photocurrent is derived and it consists of a dc component and a rf signal oscillating at the modulation frequency, which can be written as

$$I = I_{\text{dc}} + I_{\text{ac}}^{\Omega}, \tag{A5}$$

$$I_{\text{dc}} = E_0^2 \sum_{n=-\infty}^{+\infty} \left[\left(aJ_n^o\right)^2 + \left(bJ_n^e\right)^2 + 2abJ_n^o J_n^e \cos\Delta\phi\right] \times |F(\omega + n\Omega)|^2, \tag{A6}$$

$$I_{\text{ac}}^{\Omega} = 2E_0^2\{\text{Re}[AF(\omega)F^{*}(\omega+\Omega) - A^{*}F^{*}(\omega)F(\omega-\Omega)] \times \cos\Omega t + \text{Im}[AF(\omega)F^{*}(\omega+\Omega) - A^{*}F^{*}(\omega)F(\omega-\Omega)] \times \sin\Omega t + T_{\text{high}}\}, \tag{A7}$$

where

$$A = a^2 J_0^o J_1^o + b^2 J_0^e J_1^e + ab\left(J_0^o J_1^e + J_0^e J_1^o\right)\cos\Delta\phi - iab\left(J_0^o J_1^e - J_0^e J_1^o\right)\sin\Delta\phi. \tag{A8}$$

In arriving at the expressions (A6) and (A7), a unit gain of the photodetection is assumed.

APPENDIX B: THE SIMPLIFIED PDH SIGNAL FOR A HIGH-FINESSE CAVITY WITH FAST MODULATION

In contrast to a low-finesse cavity, the transfer function of a high-finesse cavity varies rapidly only near its resonances ($\gamma \ll \Delta\nu_{\text{FSR}}$, where γ and $\Delta\nu_{\text{FSR}}$ are the linewidth and FSR of the cavity). When the frequency detuning $\Delta\omega$ is much smaller than the free spectral range of the cavity ($\Delta\omega \ll 2\pi\Delta\nu_{\text{FSR}}$), the reflectance of the cavity [Eq. (6)] can be approximated as

$$F_r(\omega) \approx \frac{2r_1^2 + t_1^2}{2r_1} - \frac{t_1^2(1+r_1r_2)}{2r_1(1-r_1r_2)}\frac{1}{1+\left(\frac{\Delta\omega}{\pi\gamma}\right)^2} - i\frac{t_1^2 r_2}{\sqrt{r_1r_2}(1-r_1r_2)}\frac{\Delta\omega/\pi\gamma}{1+\left(\frac{\Delta\omega}{\pi\gamma}\right)^2}, \quad \Delta\omega \ll 2\pi\Delta\nu_{\text{FSR}}. \tag{B1}$$

In particular, when the laser frequency is tuned far from the cavity resonance ($\Delta\omega \gg 2\pi\gamma$), the reflectance is close to a constant,

$$F_{\text{roff}} = r_1\left(1 + \frac{{t_1}^2}{2{r_1}^2}\right). \tag{B2}$$

When a fast modulation of $\Omega \gg 2\pi\gamma$ is considered, except for the special case of Ω being the integer multiple of $2\pi\Delta\nu_{\text{FSR}}$, it is always satisfied that the two sidebands are far from the cavity resonance as the carrier enters the envelope of the cavity resonance. In this case the kernel of the generalized PDH signal [Eq. (2)] can be evaluated using the approximation

$$\begin{aligned} &AF_r(\omega){F_r}^{*}(\omega+\Omega) - A^{*}{F_r}^{*}(\omega)F_r(\omega-\Omega) \\ &\approx F_{\text{roff}}\{2\text{Im}[AF_r(\omega)]i - A^{*}F_r(\omega-\Omega) \\ &\quad + AF_r^{*}(\omega+\Omega) - 2F_{\text{roff}}\text{Im}[A]i\}. \end{aligned} \tag{B3}$$

Inserting Eqs. (B1) and (B3) into Eq. (2), the explicit expressions for the PDH signal are derived and the results are given by Eqs. (7) and (8) for the dispersion and absorption signals, respectively. Note that at frequencies far from resonance, the high-order term T_{high} in Eq. (2) can be simplified to

$$T_{\text{high}} = 2{F_{\text{roff}}}^2[abJ_1(M)\sin\Delta\phi - \text{Im}(A)]\sin\phi_{\text{mod}}, \tag{B4}$$

which only contributes to the dispersion term in the PDH signal.

APPENDIX C: DEMODULATED RAM SIGNALS IN THREE REPRESENTATIVE CASES

To simplify the analysis but still retain their major effects, parasitic étalons in PDH-locking optics can be divided into three categories according to their locations (cf. Fig. 5). By using Eq. (2) and the joint transfer functions given in Table I, the RAM-generated signals in three cases can be derived. When the laser frequency is locked to the optical cavity, the signals in cases (a) and (b) are separately given by

$$V_{\text{RAM}a} \approx -{E_0}^2 G_{oe}\sin\phi_{\text{mod}}\, F_{\text{roff}} F_r(\omega_0)\text{Im}[AF_{et}(\omega_0){F_{et}}^{*}(\omega_0+\Omega) - A^{*}{F_{et}}^{*}(\omega_0)F_{et}(\omega_0-\Omega)], \tag{C1}$$

and

$$V_{\text{RAM}b} \approx -{E_0}^2 G_{oe}\sin\phi_{\text{mod}}\, F_{\text{roff}} F_r(\omega_0)\text{Im}\left[A{F_{et}}^2(\omega_0){F_{et}}^{2*}(\omega_0+\Omega) - A^{*}{F_{et}}^{2*}(\omega_0){F_{et}}^2(\omega_0-\Omega)\right]. \tag{C2}$$

In case (c) the signal consists of three parts:

$$V_{\text{RAM}c} \approx V_{\text{RAM}b} + V_{\text{RAM}r} + V_{\text{RAM}rt}, \tag{C3}$$

where the first term on the right-hand side is just the signal obtained in case (b), and the last two terms are given by

$$V_{\text{RAM}r} \approx -E_0^2 G_{oe}\sin\phi_{\text{mod}}\,\text{Im}[AF_{er}(\omega_0){F_{er}}^{*}(\omega_0+\Omega) - A^{*}{F_{er}}^{*}(\omega_0)F_{er}(\omega_0-\Omega)], \tag{C4}$$

$$\begin{aligned} V_{\text{RAM}rt} \approx -E_0^2 G_{oe}\sin\phi_{\text{mod}}\,\{&F_{\text{roff}}\text{Im}\left[AF_{er}(\omega_0){F_{et}}^{2*}(\omega_0+\Omega) - A^{*}{F_{er}}^{*}(\omega_0){F_{et}}^2(\delta_{\omega_0}-\Omega)\right] \\ &+ F_r(\omega_0)\text{Im}\left[A{F_{et}}^2(\omega_0){F_{er}}^{*}(\omega_0+\Omega) - A^{*}{F_{et}}^{2*}(\omega_0)F_{er}(\omega_0-\Omega)\right]\}. \end{aligned} \tag{C5}$$

Here $V_{\mathrm{RAM}r}$ is the contribution from the field directly reflected by the parasitic étalon and $V_{\mathrm{RAM}rt}$ has its root of the interference between the two fields that are, respectively, reflected by the parasitic étalon and the optical cavity.

As illustrated in Figs. 5(a) and 5(b), in an active control scheme the RAM is detected before light enters the optical cavity. The demodulated signal in this separate path is

$$V_{\mathrm{RAM}sep} \approx -\,{E_0}^2 G_{oe} \sin\phi_{\mathrm{mod}}\, F_{\mathrm{roff}} \mathrm{Im}[A F_{et}(\omega_0) {F_{et}}^*(\omega_0+\Omega) - A^* {F_{et}}^*(\omega_0) F_{et}(\omega_0-\Omega)] = V_{\mathrm{RAM}a}/F_r(\omega_0), \tag{C6}$$

which is just the signal in case (a) divided by the on-resonance cavity reflectance $F_r(\omega_0)$.

[1] R. W. P. Drever, J. L. Hall, F. V. Kowalski, J. Hough, G. M. Ford, A. J. Munley, and H. Ward, Appl. Phys. B **31**, 97 (1983).
[2] E. D. Black and R. N. Gutenkunst, Am. J. Phys. **71**, 365 (2003).
[3] J. Hough and S. Rowan, J. Opt. A: Pure Appl. Opt. **7**, S257 (2005).
[4] T. Accadia *et al.*, J. Instrum. **7**, P03012 (2012).
[5] R. X. Adhikari, Rev. Mod. Phys. **86**, 121 (2014).
[6] The LIGO Scientific Collaboration, Nat. Phys. **7**, 962 (2011).
[7] J. Aasi *et al.* (LIGO and Virgo Collaboration), Phys. Rev. Lett. **113**, 231101 (2014).
[8] F. Acernese *et al.*, Class. Quantum Grav. **32**, 024001 (2015).
[9] S. Barke, Y. Wang, J. J. E. Delgado, M. Trobs, G. Heinzel, and K. Danzmann, Class. Quantum Grav. **32**, 095004 (2015).
[10] P. Canizares, S. E. Field, J. Gair, V. Raymond, R. Smith, and M. Tiglio, Phys. Rev. Lett. **114**, 071104 (2015).
[11] M. Takamoto, F.-L. Hong, R. Higashi, and H. Katori, Nature **435**, 321 (2005).
[12] W. H. Oskay, S. A. Diddams, E. A. Donley, T. M. Fortier, T. P. Heavner, L. Hollberg, W. M. Itano, S. R. Jefferts, M. J. Delaney, K. Kim, F. Levi, T. E. Parker, and J. C. Bergquist, Phys. Rev. Lett. **97**, 020801 (2006).
[13] T. Rosenband, D. B. Hume, P. O. Schmidt, C. W. Chou, A. Brusch, L. Lorini, W. H. Oskay, R. E. Drullinger, T. M. Fortier, and J. E. Stalnaker, Science **319**, 1808 (2008).
[14] A. D. Ludlow, T. Zelevinsky, G. K. Campbell, S. Blatt, M. M. Boyd, M. H. G. de Miranda, M. J. Martin, J. W. Thomsen, S. M. Foreman, J. Ye, T. M. Fortier, J. E. Stalnaker, S. A. Diddams, Y. Le Coq, Z. W. Barber, N. Poli, N. D. Lemke, K. M. Beck, and C. W. Oates, Science **319**, 1805 (2008).
[15] C. W. Chou, D. B. Hume, J. C. J. Koelemeij, D. J. Wineland, and T. Rosenband, Phys. Rev. Lett. **104**, 070802 (2010).
[16] N. Hinkley, J. A. Sherman, N. B. Phillips, M. Schioppo, N. D. Lemke, K. Beloy, M. Pizzocaro, C. W. Oates, and A. D. Ludlow, Science **341**, 1215 (2013).
[17] B. J. Bloom, T. L. Nicholson, J. R. Williams, S. L. Campbell, M. Bishof, X. Zhang, W. Zhang, S. L. Bromley, and J. Ye, Nature **506**, 71 (2014).
[18] W. Zhang, M. J. Martin, C. Benko, J. L. Hall, J. Ye, C. Hagemann, T. Legero, U. Sterr, F. Riehle, G. D. Cole, and M. Aspelmeyer, Opt. Lett. **39**, 1980 (2014).
[19] L. Li, F. Liu, C. Wang, and L. Chen, Rev. Sci. Instrum. **83**, 043111 (2012).
[20] H. Müller, S. Herrmann, T. Schuldt, M. Scholz, E. Kovalchuk, and A. Peters, Opt. Lett. **28**, 2186 (2003).
[21] C. Ishibashi, J. Ye, and J. L. Hall, in *Quantum Electronics and Laser Science Conference, Long Beach, California, 2002*, edited by H. Gibbs, D. Wineland, D. Gammon, and D. Heinzen, (Optical Society of America, Washington, DC, 2002), p. 91.
[22] N. C. Wong and J. L. Hall, J. Opt. Soc. Am. B **2**, 1527 (1985).
[23] E. A. Whittaker, M. Gehrtz, and G. C. Bjorklund, J. Opt. Soc. Am. B **2**, 1320 (1985).
[24] J. Sathian and E. Jaatinen, Appl. Opt. **51**, 3684 (2012).
[25] T. Kessler, C. Hagemann, C. Grebing, T. Legero, U. Sterr, F. Riehle, M. J. Martin, L. Chen, and J. Ye, Nat. Photonics **6**, 687 (2012).
[26] S. Häfner, S. Falke, C. Grebing, S. Vogt, T. Legero, M. Merimaa, C. Lisdat, and U. Sterr, Opt. Lett. **40**, 2112 (2015).
[27] K. Kokeyama, K. Izumi, W. Z. Korth, N. Smith-Lefebvre, K. Arai, and R. X. Adhikari, J. Opt. Soc. Am. A **31**, 81 (2014).
[28] L. F. Li, H. Shen, J. Bi, C. Wang, S. S. Lv, and L. S. Chen, Appl. Phys. B **117**, 1025 (2014).
[29] M. Gehrtz, W. Lenth, A. T. Young, and H. S. Johnston, Opt. Lett. **11**, 132 (1986).
[30] H. C. Sun and E. A. Whittaker, Appl. Opt. **31**, 4998 (1992).
[31] D. Xu, J. Wang, M. Li, H. Lin, R. Zhang, Y. Deng, Q. Deng, X. Huang, M. Wang, L. Ding, and J. Tang, Opt. Express **18**, 6621 (2010).
[32] E. Jaatinen, D. J. Hopper, and J. Back, Meas. Sci. Technol. **20**, 025302 (2009).
[33] J. Sathian and E. Jaatinen, Opt. Express **21**, 12309 (2013).
[34] M. T. Hartman, V. Quetschke, D. B. Tanner, D. H. Reitze, and G. Mueller, Opt. Express **22**, 28327 (2014).
[35] K. L. Dooley, M. A. Arain, D. Feldbaum, V. V. Frolov, M. Heintze, D. Hoak, E. A. Khazanov, A. Lucianetti, R. M. Martin, G. Mueller, O. Palashov, V. Quetschke, D. H. Reitze, R. L. Savage, D. B. Tanner, L. F. Williams, and W. Wu, Rev. Sci. Instrum. **83**, 033109 (2012).
[36] F. du Burck, O. Lopez, and A. El Basri, IEEE Trans. Instrum. Meas. **52**, 288 (2003).
[37] K. Ruxton, A. L. Chakraborty, W. Johnstone, M. Lengden, G. Stewart, and K. Duffin, Sens. Actuators, B **150**, 367 (2010).
[38] Y. Cao, W. Jin, H. L. Ho, L. Qi, and Y. H. Yang, Appl. Phys. B **109**, 359 (2012).
[39] Z. Li, L. Zhao, W. Tan, W. Ma, G. Zhao, X. Fu, L. Dong, L. Zhang, W. Yin, and S. Jia, Sens. Actuators, B **196**, 23 (2014).
[40] E. Jaatinen and D. J. Hopper, Opt. Lasers Eng. **46**, 69 (2008).
[41] V. Negnevitsky and L. D. Turner, Opt. Express **21**, 3103 (2013).
[42] J. Ye, L. S. Ma, and J. L. Hall, Opt. Lett. **21**, 1000 (1996).
[43] J. Ye, L. S. Ma, and J. L. Hall, J. Opt. Soc. Am. B **15**, 6 (1998).
[44] H. Dinesan, E. Fasci, A. Castrillo, and L. Gianfrani, Opt. Lett. **39**, 2198 (2014).
[45] E. D. Black, Am. J. Phys. **69**, 79 (2001).
[46] A. E. Siegman, *Lasers* (University Science Books, Sausalito, CA, 1986).
[47] D. Meschede, *Optics, Light and Lasers: The Practical Approach to Modern Aspects of Photonics and Laser Physics* (Wiley, Hoboken, NJ, 2007).

[48] A. Yariv and P. Yeh, *Photonics: Optical Electronics in Modern Communications*, 6th ed. (Oxford University Press, New York, 2006).

[49] M. Zhu and J. L. Hall, Frequency stabilization of tunable lasers, in *Atomic, Molecular, and Optical Physics: Electromagnetic Radiation*, edited by F. B. Dunning and R. G. Hulet (Academic Press, San Diego, 1997).

[50] F. Riehle, *Frequency Standards: Basics and Applications* (Wiley, Hoboken, NJ, 2006).

[51] D. N. Nikogosian, *Nonlinear Optical Crystals: A Complete Survey* (Springer, New York, 2005).

[52] K. Moutzouris, G. Hloupis, I. Stavrakas, D. Triantis, and M. H. Chou, Opt. Mater. Express **1**, 458 (2011).